ASME Journal of Mechanical Design
Online journal at:
https://asmedigitalcollection.asme.org/mechanicaldesign

Design and Examination of Compound Planetary Gearboxes to Investigate the Impact of 3D-Printed Embedded Bearings for Assistive Exoskeletons Actuators

Riccardo Bezzini[1]
Institute of Mechanical Intelligence,
Department of Excellence in Robotics and AI,
Sant'Anna School of Advanced Studies,
56127 Pisa, Italy
e-mail: riccardo.bezzini@santannapisa.it

Giulia Bassani
Institute of Mechanical Intelligence,
Department of Excellence in Robotics and AI,
Sant'Anna School of Advanced Studies,
56127 Pisa, Italy
e-mail: giulia.bassani@santannapisa.it

Carlo Alberto Avizzano
Institute of Mechanical Intelligence,
Department of Excellence in Robotics and AI,
Sant'Anna School of Advanced Studies,
56127 Pisa, Italy
e-mail: carloalberto.avizzano@santannapisa.it

Alessandro Filippeschi
Institute of Mechanical Intelligence,
Department of Excellence in Robotics and AI,
Sant'Anna School of Advanced Studies,
56127 Pisa, Italy
e-mail: alessandro.filippeschi@santannapisa.it

In robotic systems such as wearable exoskeletons, lightweight, efficient, and backdrivable reduction gearboxes are critical for achieving low-output impedance actuators and safe physical human–robot interaction. Recent trends in robotics research highlight the growing adoption of 3D-printed gearboxes, which enable rapid prototyping, flexibility, and lightweight solutions. However, these reducers can still exhibit significant weight and encumbrance, mainly due to the reliance on conventional bearings that add substantial bulk and mass. In this article, we design and experimentally evaluate two 3D-printed 1:30 compound planetary reducers. The first prototype employs standard bearings, while the second integrates 3D-printed bearing guides composed of steel rollers moving through custom polymer raceways embedded in the gearbox components. This approach aims at diminishing the reducer's overall cost, weight, and encumbrance, while retaining key mechanical performance characteristics. Experimental results show that the proposed 3D-printed bearing solution reduces gearbox weight by approximately 32% and manufacturing cost by about 33% compared to the bearing-based counterpart. Moreover, the reducer achieves a backdrive torque as low as 0.42 ± 0.06 N m, representing the lowest value among the compared designs, together with a marked reduction in internal friction. Despite the replacement of conventional bearings with fully integrated printed guides, the gearbox preserves comparable gear play and stiffness while improving backdriveability and speed regularity. These results demonstrate that fully customized, additively manufactured reducers with embedded bearing systems can provide substantial mechanical and integration advantages for lightweight wearable robotic actuators.
[DOI: 10.1115/1.4071656]

Keywords: exoskeleton actuators, compound planetary reducer, 3D-printed bearings

1 Introduction

Wearable exoskeletons are assistive robotic systems that augment human motion, addressing both lower and upper limbs, by providing powered support for locomotion and manipulation tasks in contexts ranging from mobility assistance to physical augmentation and rehabilitation [1–3]. Achieving seamless and intuitive physical human–robot interaction (pHRI) in such systems necessitates the integration of actuation units characterized by low mechanical output impedance, high intrinsic back-drivability, and minimal reflected inertia [4,5]. These characteristics are critical to ensure compliant interaction with the user's natural biomechanics while maintaining responsiveness, comfort, and safety. Moreover, the entire actuator assembly must conform to constraints on size, weight, and form factor to preserve wearability and ergonomic compatibility with the human body, thus improving transparency in the human-exoskeleton coupled system [6,7]. A critical aspect in accomplishing these features lies in the transmission systems' design. Reduction gearboxes are responsible for converting the motor output into high-torque mechanical power needed at the exoskeleton's joints. For wearable robotic applications, the transmission system design should aim for a reducer that is lightweight, compact, mechanically efficient, cost-effective, and backdrivable. Achieving this balance of performance and integration is a fundamental challenge in exoskeleton actuation design [8].

Various transmission technologies have been explored to fulfill the stringent requirements of wearable robotic actuation. Quasi-

[1]Corresponding author.

Contributed by the Power Transmission and Gearing Committee of ASME for publication in the Journal of Mechanical Design. Manuscript received November 3, 2025; final manuscript received April 5, 2026; published online April 27, 2026. Assoc. Editor: Alfonso Fuentes-Aznar.

direct drive systems provide excellent torque transparency and back-drivability [9,10], but since they employ low reduction ratio reducers, they are inherently limited in their torque output, making them less suitable for high-assistive applications. This actuation paradigm usually involves the use of cycloidal [11] and planetary gearboxes [12] or their combination in multiple-stage designs [13]. In cases of higher torque requirements, harmonic drive gearboxes are employed, since they allow for the implementation of high reduction ratios in compact volumes [14]. However, these reducers often suffer from low backdriveability and increased hysteresis under varying loads [15].

Recently, compound planetary reducers have gained attention as a promising alternative to the mentioned systems, offering several key advantages: they enable high overall reduction ratios through multiple gear stages while maintaining coaxial symmetry, resulting in a compact and well-balanced form factor [16]. Additionally, these architectures provide low gear backlash, high transmission efficiency, and smooth torque output with minimal ripple. Their distributed load-sharing and favorable contact mechanics also contribute to improved back-drivability compared to other high-ratio systems [17,18]. Despite these benefits, the use of compound planetary systems in wearable applications still presents challenges related to overall weight and encumbrances. Recent trends in robotic applications address these issues through the employment of 3D-printed gearboxes [13,19,20]. In previous works, a 1:30 3D-printed compound planetary reducer was designed and evaluated for assessing its employment in exoskeleton actuation [21]. While the reducer achieved promising torque-handling and back-driveability capabilities, its total weight and radial dimensions were significantly affected by the use of conventional metallic bearings. These off-the-shelf components contributed disproportionately to the mass and spatial encumbrance of the 3D-printed gearbox, limiting its employment for lightweight and tightly packaged wearable systems.

To overcome these limitations, this work explores the potential of custom 3D-printed bearing guides integrated directly into the components of compound planetary reducers. By replacing conventional ball bearings with polymer-based printed channels and embedded steel spheres, the goal is to achieve significant reductions in weight, cost, and encumbrance while preserving the mechanical functionality required for actuating wearable robots. This approach exploits the geometric flexibility of additive manufacturing to create fully customized interfaces between rotating elements, enabling the embedment of customized guides for rolling elements in the components of the reduction gearbox. In the literature, various approaches for the design and analysis of 3D-printed bearings have been explored, spanning from printed textured journal bearings [22] to fully printed components [23,24], including the investigation of the damping characteristics of bearings manufactured employing hybrid materials [25,26]. Although 3D-printed reducers have been widely explored in recent years, to assess the value of different architectures [12,27] and evaluate the impact of printed components with respect to metal parts [20], to the authors' knowledge, there is no evidence in the literature of any studies proposing, investigating, or analyzing the impact of 3D-printed bearings on reduction gearboxes.

In this article, we employ 3D-printed guides for steel rolling elements to embed customized bearings in a printed planetary compound reduction gearbox. To evaluate the feasibility and performance of this approach, two 1:30 reducer prototypes were designed, fabricated through 3D printing, and tested. The first prototype retains the conventional bearing-based design, using standard steel ball bearings for all rotational interfaces. The second prototype introduces integrated 3D-printed bearing guides, fully embedding the rolling elements within the polymer structure of the housing and ring gears. This comparative setup enables a direct assessment of printed bearings' impact on the transmission's performance, allowing us to identify potential trade-offs in efficiency, stiffness, and torque transmission, and to determine the overall value and viability of a fully 3D-printed reducer for assistive exoskeleton applications. Given the nonlinear mechanical behavior and potential compliance of polymer materials under load, experimental validation of these printed prototypes is essential. Analytical models would not be sufficient for accurately predicting their stiffness, frictional behavior, or long-term durability, especially under dynamic loading conditions and tasks.

The novelty of this study lies in the combination of a proven 3D-printed compound planetary architecture with integrated, custom-designed 3D-printed bearing systems, forming a fully additively manufactured transmission solution, with the exception of the smallest bearings. This approach directly addresses the limitations of the original reducer design—primarily related to weight, cost, and encumbrance—by replacing bulky metal bearings with lightweight, embedded polymer-based alternatives. As a result, the overall system becomes more suitable for tight, weight-sensitive integration in wearable actuation modules, such as those used in assistive exoskeletons [28].

In this work, we present the design, development, and fabrication of two novel lightweight reducers specifically conceived for assistive exoskeleton applications. Their performance is systematically evaluated according to key metrics for the characterization of transmission systems, namely friction, gear play, gear stiffness (GS), backdrivability, speed regularity, as well as size, weight, and cost.

The results not only validate the mechanical viability of the printed bearing solution but also demonstrate that the fully 3D-printed reducer can outperform state-of-the-art transmission systems, further enforcing its applicability to real-world wearable assistive robots. This work highlights how the strategic use of additive manufacturing can improve transmission performance while drastically reducing production complexity, weight, cost, and integration constraints.

To sum up, the main contributions of this article are as follows:

- The introduction of custom 3D-printed bearing guides into a reducer's design to reduce weight, cost, and spatial encumbrance while maintaining acceptable mechanical performance.
- The design and development of two 3D-printed 1:30 compound planetary reducers, one employing classic bearings, while the other embeds 3D-printed guides for steel spherical rollers. Computer-aided design (CAD) files and BOM (Bill of Materials) are available in Ref. [29].
- An experimental investigation assessing the impact of the 3D-printed bearing solution on friction, gear play, stiffness, backdriveability, and mechanical stability across key operational metrics, to assess the value of the prototypes for actual wearable assistive devices.

The rest of this article is structured as follows: Sec. 2 presents a brief description of the planetary compound architecture, then describes the customized 3D-printed bearing structure employed, and subsequently illustrates the gearboxes designed and developed for this work. Next, the experimental setup, metrics, and protocols are presented. Section 2.2 explicates the results and the evaluative considerations of the experimental analysis, discussing the different features of the investigated reducers and providing an overall examination of the advantages and limitations of the presented work. Finally, Sec. 4 presents a conclusive summary of the proposed work, summarizing the most relevant insights.

2 Materials and Methods

2.1 Proposed Design. This work presents the design of two 3D-printed compound planetary reducers developed to address key limitations of the 1:30 gearbox from previous work [21], which already proved more lightweight and less bulky than other state-of-the-art 3D-printed planetary gearboxes [18,30]. Aiming for the same 1:30 reduction ratio, the design constraints for radial and axial encumbrance were set, respectively, to 90 mm and 50 mm, thus reducing the reported gearbox dimensions from previous studies.

Both prototypes aim to reduce bulk and mass while preserving the mechanical functionality required for wearable exoskeletons' actuation. The first, CFB (compound full bearings), revisits the original metallic-bearing configuration but improves the geartrain layout to reduce volume and mass through a revised gear teeth distribution. The second, C3D (compound 3D-printed), introduces a novel design featuring integrated 3D-printed bearing guides for steel rolling elements, enabling a fully embedded, lightweight, and cost-effective alternative to commercial ball bearings.

This approach differs from previous additive manufacturing efforts in printed rolling elements bearing systems—developed using polymeric rollers [23]—which were limited to proof-of-concept experiments without an application to gearbox use cases. By embedding steel spheres within printed polymer channels, the proposed bearing system leverages the geometric adaptability of additive manufacturing while retaining the load-carrying capabilities of classic bearings. The result is a customizable bearing interface with significantly lower spatial and weight impact, removing dependency on bulky, off-the-shelf components and paving the way for tightly integrated wearable actuators.

2.1.1 Compound Planetary Architecture. To address the limitations of standard planetary gearboxes in reaching high reduction ratios, the compact epicyclic arrangements introduced in Ref. [31] provide designs that allow significantly higher gear ratios. This architecture, shown in Fig. 1, is a combination of two planetary stages (A and B). However, unlike the traditional planetary design, this compound transmission utilizes two ring gears: the first one (stage A) is fixed, while the second ring gear (stage B) is the reducer's output. The input shaft moves the stage A sun, whereas stage B does not include a sun gear. The compound planets are composed of two different base planets rigidly connected to form a single component. For each compound planet, the base gears that compose it are combined with different multiples of a rotation angle, computed for each stage based on the number of teeth of each gear (see Ref. [31] for the details). The resulting reduction ratio can be computed according to the following equation:

$$i = \frac{1 + \dfrac{z_{ra}}{z_{sa}}}{1 - \dfrac{z_{pb} z_{ra}}{z_{pa} z_{rb}}} \tag{1}$$

where z_{ij} denotes the number of teeth of a general gear, and the subscripts consist of $i \in \{s, p, r\}$ (these numbers denote the sun, planet, and ring, respectively) and $j \in \{a, b\}$ (these letters denote the first and second planetary stages, respectively).

2.1.2 Three-Dimensional-Printed V-Shaped Races Bearings. To develop a fully printed reduction gearbox, the custom polymeric bearings should be able to resist both radial and axial loads. The typical round-shaped groove design would require deep channels and, therefore, wider rolling elements. Since the main objective of our design is to minimize encumbrances and weight, this option was not applicable. For this reason, a V-shape design has been selected for the 3D-printed bearings to be embedded in the reducer's structure. A CAD section view of the employed model for the printed races is presented in Fig. 2. The same design has been employed for all the printed guides. While the employed steel balls' diameter is 3 mm, for printing races that could contain these rollers and move freely (nonetheless without axial or radial play), during the design, the roller's diameter was considered 3.05 mm.

2.1.3 Presented Gearboxes: Compound Full Bearings and Compound 3D-Printed. From Eq. (1), a desired reduction ratio is realizable with multiple combinations of tooth numbers: varying the number of teeth and their module clearly impacts the resulting radial encumbrance. For printability issues and for allowing a fair comparison with the CO30 prototype from previous work [21], the

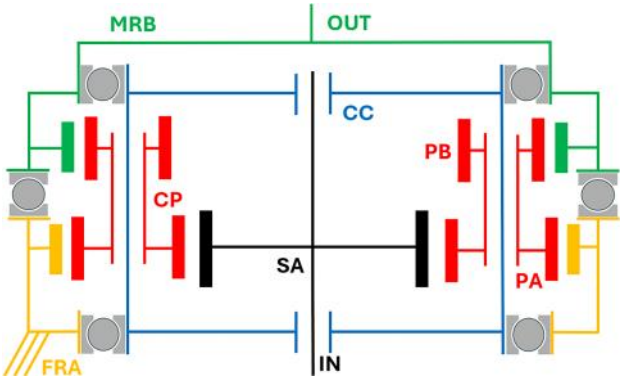

Fig. 1 Schematic illustration of the structure of the planetary compound (CO) reducer. The acronyms used represent the role of the different parts. IN denotes the input shaft, which corresponds to the stage A planetary sun SA. FRA refers to the planetary fixed stage A ring. CP denotes the compound planets, composed of two joint gears, i.e., PA and PB, respectively, the planet of stage A and the planet of stage B. CC refers to the compound carrier to which the planets are connected. MRB refers to the stage B planetary moving ring, which corresponds to the reducer's output. The bearings (connecting the fixed and moving rings between themselves and with the carrier) are the ones addressed in the following and substituted with 3D-printed guides and spherical rollers.

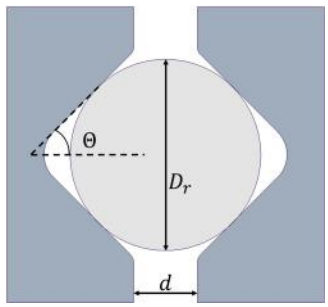

Fig. 2 CAD section view of the proposed design for the printed bearings, employing a V-shape race and spherical rollers. The angle Θ defines the inclination of the races' contact surfaces. The roller diameter is denoted as D_r, while d represents the clearance left between the inner and outer rings of the 3D-printed bearing.

Table 1 Design parameters of the presented compound planetary prototypes

Parameter	Value
Number of teeth ring A (z_{ra})	48
Number of teeth planets A (z_{pa})	16
Rotation angle planets A	90 deg
Number of teeth sun A (z_{sa})	16
Number of teeth ring B (z_{rb})	45
Number of teeth planets B (z_{pb})	13
Rotation angle planets B	131.54 deg
Number of planets	4
Teeth module	1.2 mm
Teeth pressure angle	25 deg
Carrier radius	19.2 mm
Rollers diameter (D_r)	3 mm
Races contact surface inclination (Θ)	45 deg
External–internal bearing rings distance (d)	1 mm

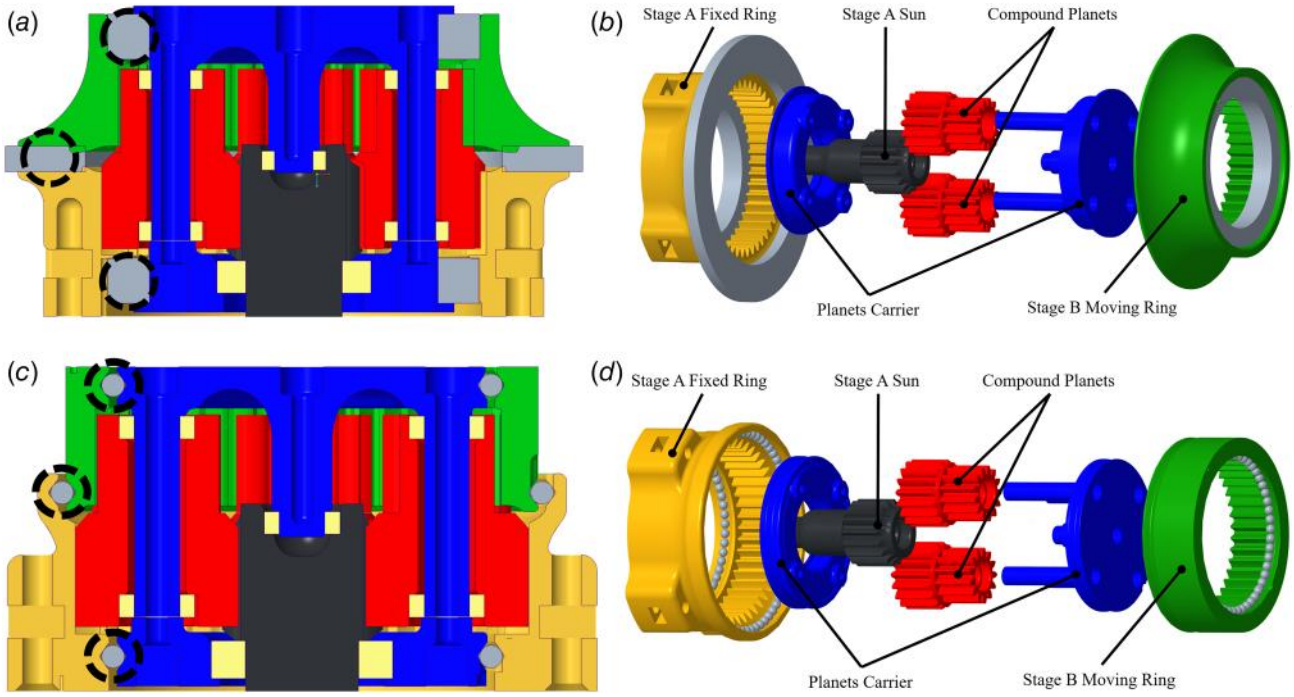

Fig. 3 Section and exploded views of the CAD models of the CFB (*a* and *b*) and C3D (*c* and *d*) planetary compound reducers. Nuts and screws are not shown for better comprehensibility of the figure. The structure of the illustrated parts corresponds to the one employed in Fig. 1. In the section views, the bearings that are substituted by 3D-printed ones are highlighted with dashed circles. In the exploded views, only two out of four planets are displayed to improve the figures' comprehensibility, and the main components are labeled. The displayed parts include the output stage B ring gear, the compound planets, the stage A fixed ring, the stage A sun gear, and the carrier. The smaller bearings are depicted in light grey, while the larger ones (i.e., those replaced by 3D-printed races in the C3D device) and the rolling elements in C3D are highlighted by dashed circles. (*a*) Section view of the CFB prototype's CAD model. (*b*) Exploded view of the CFB prototype's CAD model. (*c*) Section view of the C3D prototype's CAD model. (*d*) Exploded view of the C3D prototype's CAD model.

same teeth module has been employed (i.e., 1.2 mm). Given these conditions, we managed to achieve a teeth combination that met the mentioned constraints. As can be noticed from Table 1, where all the main parameters of the presented reducers are reported, the two prototypes have been designed employing the same variables (clearly, the details regarding the 3D-printed races' geometry only concern the C3D device). This allowed for an experimental evaluation to detect the effects of the 3D-printed bearings on the selected metrics. Figure 3 presents the CAD views of the CFB and C3D prototypes sections (screws and nuts are not displayed to avoid overloading the figure), highlighting the differences due to the implementation of the 3D-printed bearings.

The CFB still incorporates standard ball bearings at all rotational interfaces. The two bearings between the ring gears and the carrier, and the trust bearing that connects the two ring gears with each other, are the bigger ones, therefore the ones that impact weight and cost the most. In the C3D prototype, these components are replaced with the printed custom polymer tracks designed to house loose steel spheres as rolling elements. These guides, as can be noted from Fig. 3, are embedded directly within the reducer's ring gears and carrier structures, forming continuous raceways tailored to the specific spatial requirements of the transmission layout.

Table 2 reports all the bearings and rollers employed for the two prototypes, showing the substitutions implemented in the C3D gearbox through the 3D-printed V-shaped races and the steel spherical rollers. The resulting reducer's design can be observed in Fig. 3, where the interested bearings and the rollers for the custom 3D-printed races are depicted in gray and highlighted to stress the differences between the two designs.

Table 2 Bearings employed for the presented CFB and C3D prototypes

Bearing connection	CFB	Quantity
Carrier—sun A	6802	1
Ring A—carrier	6809	1
Carrier—planets	MR106	8
Ring A—ring B	AXK6590	1
Carrier—ring B	6809	1
Bearing connection	**C3D**	**Quantity**
Carrier—sun A	6802	1
Ring A—carrier	3 mm rollers	40
Carrier—planets	MR106	8
Ring A—ring B	3 mm rollers	55
Carrier—ring B	3 mm rollers	40

2.1.4 Materials, Printers, and Off-the-Shelf Components. To develop the presented reducers, Ultimaker PLA (polylactic acid) was employed, given its valuable combination of low costs and significant mechanical properties [32,33]. The manufacturing process involved the use of the Ultimaker S7 Pro Bundle printer, with slicing carried out via Ultimaker Cura. The parts that were not produced through 3D printing were the bearings, steel balls, screws, and nuts. The bill of materials and CAD files of the presented prototypes are available in Ref. [29].

2.2 Experimental Evaluation. In this section, the two configurations of the experimental setup employed to evaluate the chosen metrics are described. Then, the selected performance metrics are presented, together with the respective experimental protocols (Fig. 4).

Fig. 4 Photos of the stage A rings of the two reducers assembled with the lower part of the carriers. On the left side of the two figures, the C3D prototype is shown, as can be noted from the presence of the printed races and the steel balls. These figures give a hint of the differences between the same components in the two proposed architectures.

2.2.1 Experimental Setup. The experimental setup is composed of the brushless motor (EC 90 flat, 360 W, ϕ 90 mm, Maxon, Bad Homburg, Germany), which includes an integrated two-channel encoder (MILE 512-6400 CPT, Maxon) coupled to the reducer's input shaft through the 3D-printed motor support. The reducer's output link is connected to an incremental magnetic encoder (H2 Series, Phoenix America, Fort Wayne, IN) through the 3D-printed encoder support. All the mentioned components are fixed to a horizontal aluminum beam through a 3D-printed support structure. The motor-encoder assembly is controlled by a three-phase brushless DC motor driver (STEVAL-SPIN3201, STMicroelectronics, Geneva, Switzerland). The magnetic encoder and the two load cells (CZL635, Phidgets Inc.), which can be placed in a case on the output arm if the test demands the force detection at the reducer's output, are connected to the STM32 Nucleo-144 board (NUCLEO-F767ZI, STMicroelectronics). Both these boards are connected to the central unit (Intel NUC 11 Pro, i7-1165G7) running WINDOWS 11 and SIMULINK (MATLAB, Mathworks Inc., Natick, MA), where two PID (*discrete PID controller,* SIMULINK block) controls are designed to manage the motor's position and speed, depending on the performed test. A custom Kalman filter (MATLAB function, SIMULINK block) is employed to estimate the motor speed.

Figure 5 displays the setup with photos of the two exploited experimental arrangements, addressed as EXP1 and EXP2 in the following, where the main components are illustrated and pointed out. As can be noted from these figures, the EXP1 configuration does not involve the use of the output arm, since the tests conducted in this arrangement did not include output forces or torque measurements. The output arm is composed of two 20×20 mm aluminum beams held together with some printed parts, which also include the terminal elements that are coupled with the weights employed for the tests under external loads.

2.2.2 Evaluation Metrics. To evaluate the CFB and C3D prototypes' performance (and additionally compare them with the previous design CO30 from Ref. [21]), the following metrics have been taken into consideration:

Gear play: Defined as the output angular range observable with the input shaft locked, in which no resisting torque is transmitted from the actuator. A smaller gear play reflects higher positional accuracy in motion transmission.

Gear stiffness: The gearbox's output stiffness is defined as the ratio between the applied torque at the output (with the input shaft locked) and the resulting angular displacement. This metric is relevant since higher stiffness enhances tracking accuracy in trajectory-control tasks, whereas lower stiffness provides compliance, beneficial for smoother and safer pHRI.

Backdrive torque: The torque that must be externally applied at the output shaft to initiate motor motion. This characteristic is particularly relevant for wearable actuators, which must not hinder the user's voluntary movements.

Friction: Represents the motor torque needed to counteract static (Coulomb) and dynamic (viscous) resistances opposing reducer motion. Quantifying internal friction is critical for applying compensation strategies, which in turn improve actuator transparency in pHRI.

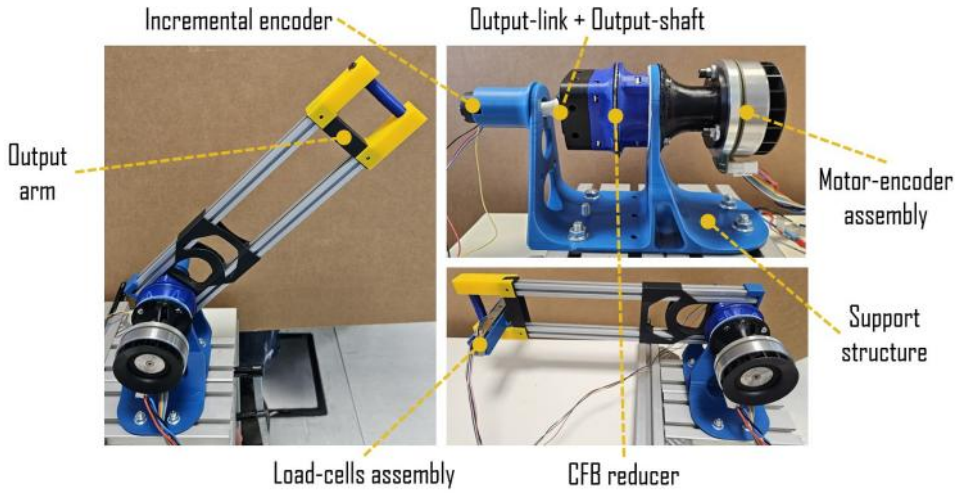

Fig. 5 Experimental apparatus for testing the reducers. The photos and notes to clarify the composition of the experimental setup, both in the configuration with and without the output arm and the load cells.

Speed regularity: Refers to the oscillatory deviation between the measured reducer output speed and its theoretical value. The latter is obtained as the product of the motor angular velocity and the transmission ratio. Assessing regularity provides insight into the stability and accuracy of speed transmission.

Size, weight, and cost: The reducers were fabricated using Ultimaker PLA, so the overall mass, bulk, and cost largely depend on the quantity and type of bearings and fasteners employed. Minimizing weight and encumbrance is crucial for wearable robotics to ensure usability and user acceptance. At the same time, maintaining low manufacturing costs while preserving mechanical performance is key to enabling large-scale adoption of assistive technologies.

2.2.3 Experimental Protocols. The presented experimental apparatus allowed testing the reducers and comparing their characteristics through the evaluation of their performances via multiple procedures.

Gear play: The gear play was quantified by measuring the maximum output displacement while keeping the motor's shaft blocked. To avoid the effect of joint stiffness, the procedure consisted of manually moving the reducer's output link without applying significant torque. The measurement was repeated at $2i$ consecutive motor positions, evenly spaced by an entire 360 deg motor rotation, to characterize the backlash over two full revolutions of the reducer's output. Each prototype was tested three times to ensure consistency of the results.

Backdrive torque: The experimental setup to identify the backdrive torque included both the output arm and the load cells. At the beginning of each test, the motor was positioned such that the output arm remained horizontal, providing a reference to correctly account for the torque contribution of the arm and load weight, which varied with the angular configuration. Forces were manually applied to the load cells in increasing magnitude until motor displacement was observed. Each test was performed at least five times and repeated in three independent sessions. Backdrive torque was then estimated by identifying motor displacement detected using a threshold of 0.18 deg, corresponding to twice the encoder resolution, and calculating the corresponding applied torque. The final torque value incorporated the manually applied forces as well as the contributions of the arm and load weights, adjusted according to the output angle.

Gear stiffness: The experimental setup involved the use of the output arm equipped with the load cells, mounted with a lever arm length of 0.43 m. Transmission stiffness was identified by manually applying an increasing series of loads to the arm, while continuously recording the load-cell force signal. Each loading session has been addressed with the name GS in the following. The maximum applied load for each reducer was approximately 55 N, corresponding to 25 N m at the output (this torque value also includes the contribution due to the weight of the arm and load cells assembly).

Each test was repeated three times per reducer, with output positions incremented by 60 deg to capture possible position-dependent variations. The resulting torque-displacement data were employed to fit a linear model to estimate the output stiffness, defined as

$$k_{\mathrm{g}} = \frac{\Delta\tau_{\mathrm{out}}}{\Delta\theta_{\mathrm{out}}} \tag{2}$$

where k_{g} denotes the gearbox stiffness, $\Delta\tau_{\mathrm{out}}$ is the applied torque at the output, and $\Delta\theta_{\mathrm{out}}$ is the corresponding angular displacement. For each loading process GSi (from 0 N m to 25 N m), the mean stiffness has been computed. Then, the mean value and standard deviation for each reducer have been calculated.

Friction: Prior to evaluating the reducers' performance, the motor's internal static and viscous friction were identified by commanding the motor to track multiple low-frequency sinusoidal speed references. The resulting current measurements were used to implement friction compensation. In addition, friction was further characterized by imposing slowly varying ramp inputs within the range of ± 150 rad/s, following the methodology reported in Ref. [27]. Each ramp profile was executed three times, and the complete procedure was repeated three times for every reducer. Given the results obtained in Ref. [21], at first, speed and torque data were then employed to attempt to fit the following asymmetric friction model:

$$\tau_{fr} = \begin{cases} M_c^+ + d_v^+ \omega_m & \text{if } \omega_m \geq 0 \\ -M_c^- + d_v^- \omega_m & \text{if} \omega_m \leq 0 \end{cases} \tag{3}$$

where τ_{fr} denotes the friction torque, M_c^+ and M_c^- denote the Coulomb friction components (respectively, for positive and negative velocities), d_v^+ and d_v^+ denote the viscous coefficients, and ω_m is the motor velocity. Representative results, including torque–speed data and the corresponding fitted model for each reducer, are presented in Fig. 8.

However, the recorded data were not compatible with the model presented in Eq. (3). Thus, we resorted to the more detailed Stribeck friction curve, modeled according to the following equation:

$$\tau_{fr} = \sqrt{2e}\,(M_{\mathrm{brk}} - M_c)\, e^{-\left(\frac{\omega}{\omega_{st}}\right)^2} \frac{\omega}{\omega_{st}} + M_c \tanh\left(\frac{\omega}{\omega_{\mathrm{coul}}}\right) + \mathrm{d}\omega \tag{4}$$

with the characteristic velocities defined as

$$\omega_{st} = v_{\mathrm{brk}}\sqrt{2}, \qquad \omega_{\mathrm{coul}} = \frac{v_{\mathrm{brk}}}{10} \tag{5}$$

where $M(v)$ is the friction moment as a function of the relative velocity v, M_{brk} is the breakaway (stiction) friction force, M_c is the Coulomb friction force, ω_{st} is the Stribeck velocity threshold, ω_{coul} is the Coulomb friction threshold velocity, v_{brk} is the breakaway velocity, and d is the viscous friction coefficient. All the mentioned velocities (referred to as ω) refer to the motor speed. This model captures the nonlinear decay of friction from the breakaway value M_{brk} toward the Coulomb level M_c as velocity increases, with ω_{st} shaping the Stribeck effect. At higher velocities, the viscous term d becomes dominant, resulting in a linear growth of friction. Figure 6 presents two illustrations of the mentioned friction models to clarify the employed notation.

Speed regularity: The regularity metric quantifies the deviation between the actual output speed of the reducer and its theoretical value, providing a measure of the actuator's capability to track a constant velocity. To evaluate unloaded regularity (R_{CFB} and R_{C3D}), a PID controller was employed to regulate the motor speed according to a sequence of step inputs ranging from 0 to ± 120 rad/s in increments of 20 rad/s (Fig. 9). For the two prototypes, each test was repeated three times for both positive and negative velocities.

Regularity was then computed as

$$R = 100\left(1 - \frac{\Delta\omega_g}{i\,\omega_m}\right) \tag{6}$$

where R denotes the regularity (expressed as %), ω_g is the measured gearbox's output speed, i represents the reduction ratio, and ω_m is the motor speed.

Size, weight, and cost: Regarding the prototypes' encumbrance, the maximum height and the diameter of the reducers were first derived from the CAD models and subsequently verified through physical measurements. It is worth remarking that the presented encumbrances report the gearboxes'

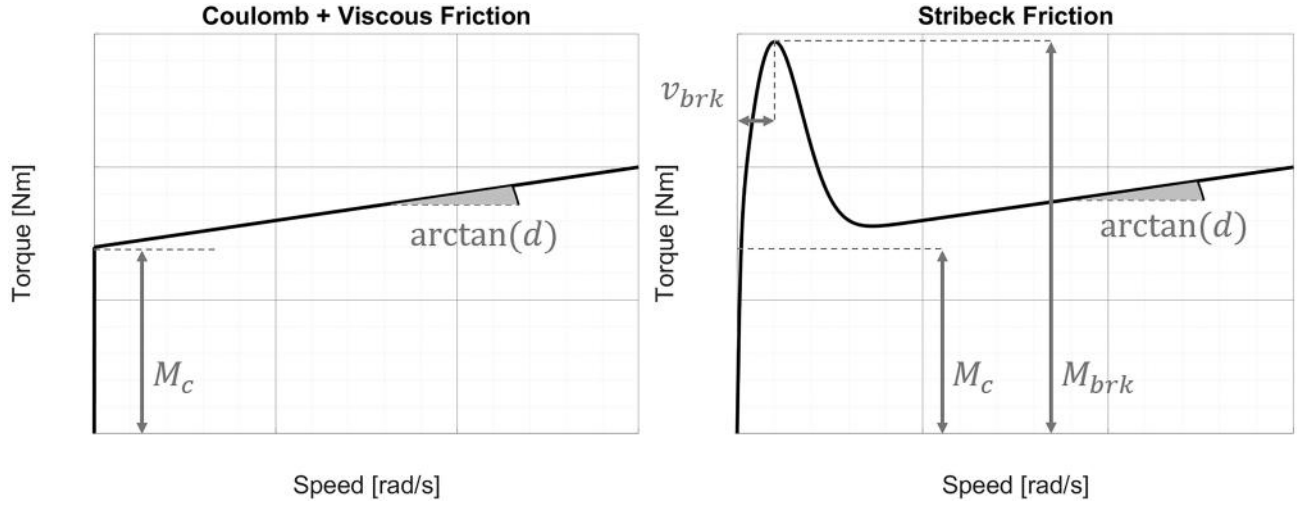

Fig. 6 Illustrations of the presented friction models. Only the positive velocities' side is represented, as for this work, we considered models that are symmetric with respect to the origin, thus equal in magnitude but opposite in sign for positive and negative velocities. On the left, the model employed in the previous work, including a Coulomb static component M_c and a viscous factor d. On the right, the Stribeck's complete friction model is represented, including the breakaway static component M_{brk} and the breakaway velocity v_{brk}.

shapes without considering the connection with the employed setup, implemented through four screws on a ϕ 70 mm circumference. Therefore, the comparison between the encumbrances does not depend on the experimental setup, but only on the prototypes' design.

The overall cost was estimated by summing the price of the nonprinted components (e.g., bearings, steel balls, screws, and nuts) with the cost of the 3D-printed parts. The cost of the PLA elements was determined based on their weight, accounting for the material price, the energy consumption during fabrication, and the amortization of the printer over its expected lifetime. For the nonprinted components, prices were obtained from the supplier's catalog and scaled according to the required quantities. In particular, bulk purchases (e.g., sets of bearings) resulted in reduced unit costs, which directly influenced the total cost of each reducer depending on the number of identical parts it included.

Finally, the total mass of each reducer was measured directly using a precision scale.

3 Results and Discussion

3.1 Gear Play. The gear play evaluation results reported in Table 3, with the best values displayed in bold text, highlight clear differences among the examined prototypes. While all three evaluated reducers display valuable gear play, the CO30 presented the highest measured backlash, with a mean value of 0.53 ± 0.21 deg. In contrast, both of the newly developed prototypes demonstrate substantially reduced gear play. In particular, the CFB prototype achieves the lowest mean backlash (0.114 ± 0.076 deg). The C3D prototype also shows a notable improvement (0.195 ± 0.084 deg).

It is worth noting that both prototypes outperform some of the state-of-the-art solutions reported in the literature [21,27,34]—where the analyzed 3D-printed reducers' best gear play values vary between 0.23 deg and 0.7 deg—thereby demonstrating the effectiveness of the presented designs.

It is also notable that the C3D achieves excellent gear play performance despite incorporating printed bearings. This demonstrates that the design of the C3D architecture effectively compensates for potential compliance or tolerances introduced by additive-manufactured components, maintaining a high level of precision comparable to the CFB. Such results highlight the robustness of the proposed designs in delivering low backlash even when using advanced manufacturing techniques.

3.2 Backdrive Torque. Regarding backdrive torque, substantial differences also emerge among the evaluated prototypes. The reference design reports a mean value of 0.67 ± 0.04 N m, while the CFB prototype shows the highest torque requirement (1.18 ± 0.019 N m). In contrast, the C3D prototype achieves the lowest backdrive torque, with a mean value of only 0.42 ± 0.063 N m, confirming its clear advantage over both the reference and the CFB implementation. Considering that the CFB and C3D prototypes implement the same gears' structure and number of teeth, it is clear that the significantly reduced internal friction (thanks to the use of 3D-printed bearing systems) manifests itself in the examined improvement of the C3D reducer's backdriveability.

With respect to other state-of-the-art reducers, C3D presents a highly valuable backdrive torque, demonstrating a significant improvement in relation to both 3D-printed gearboxes (the lowest backdrive torque, to the authors' knowledge, is the 0.59 N m backdrive torque of the CP30 and CYPLO prototypes from Refs. [13,21]) and other actuators employed in wearable devices (considering the lightweight exoskeletons presented in Ref. [10], which reports a backdrive torque of 0.97 N m in a quasi-direct drive actuator for a hip exoskeleton). Such results are particularly relevant in the context of wearable assistive devices, where backdrivability strongly influences comfort and usability. Typical assistance levels in these applications are in the range of 10–25 N m [35,36], meaning that the reported backdrive values are practically negligible in comparison. This enforces the suitability of the presented prototypes—especially the C3D—for integration into

Table 3 Results from the tests regarding gear play and backdrive torque

ID	Gear play (deg)	Backdrive torque (N m)
CO30 [21]	0.53 ± 0.21	0.67 ± 0.04
CFB	$\mathbf{0.114 \pm 0.076}$	1.18 ± 0.019
C3D	0.195 ± 0.084	$\mathbf{0.42 \pm 0.063}$

The best value for each feature is reported in bold.

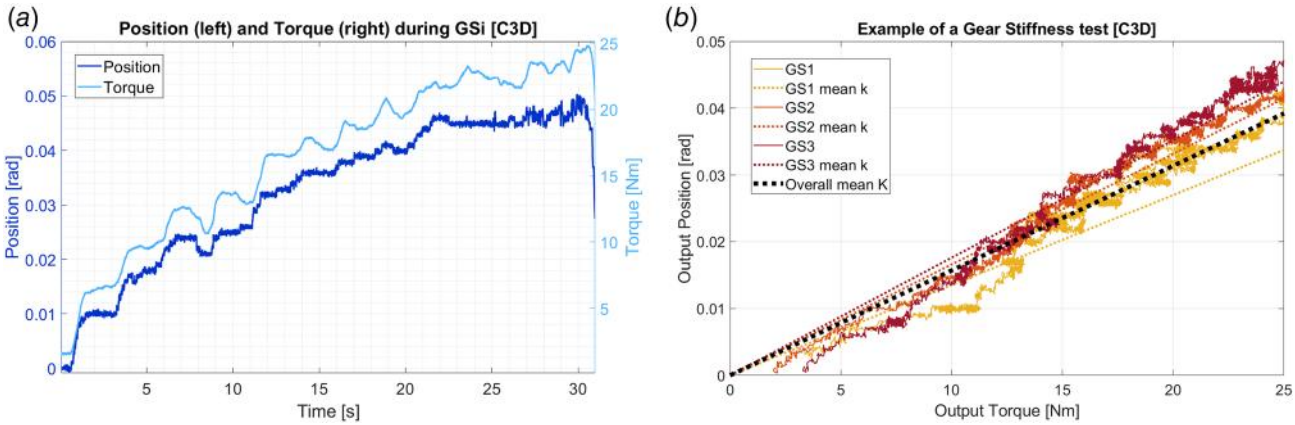

Fig. 7 Illustrations of the data gathered from a stiffness test. (*a*) Presents the output torque and angular displacement results regarding one loading session conducted on the C3D device. (*b*) Reports the angular displacement displayed as a function of the applied torque during all three GSi (loading sessions from 0 to 25 N m) of one stiffness test carried out on the C3D prototype.

Table 4 Results from the tests for the gear stiffness

ID	Gear stiffness (N m/rad)
CO30 [21]	723.2 ± 71.05
CFB	971.52 ± 108.01
C3D	653.68 ± 64.91

wearable systems, where both low gear play and low backdrive torque are crucial for ensuring natural and transparent user interaction.

3.3 Gear Stiffness. The linear fitting of the motor torque-angular displacement profiles enabled the estimation of each reducer's stiffness.

Figure 7 reports examples of the data gathered during the stiffness tests, with the related estimations of linear fitting models for evaluating the reducers' stiffnesses. As shown in the plots, the gradual increase in angular displacement as the applied torque increases indicates a relatively linear behavior. The stiffness values computed for the CFB and C3D devices are reported in Table 4.

Analyzing these numbers, the C3D reducer shows a stiffness of 653.68 ± 64.91 N m/rad, which is lower than the CFB reducer (971.52 ± 108.01 N m/rad). These values are comparable with other 3D-printed reducer stiffness [13,20,21,34], where the maximum reported stiffnesses vary between 633 N m/rad and 879 N m/rad. Moreover, both the CFB and C3D stiffnesses are well-suited for lightweight wearable assistive devices, considering the aforementioned plausible torque ranges (10–25 N m) and the range of target stiffness of state-of-the-art elastic joints [37–39]. These reducers would surely be able to provide the necessary torque output while maintaining a level of flexibility suitable for user comfort and functionality. Of course, depending on the assistive torque to be delivered by a wearable device and on the control strategy implemented at the actuated joints, the transmission system's stiffness should be taken into consideration to be compensated for or employed for plausible impedance control approaches.

3.4 Friction. The sampled motor torque and speed during the slowly ramping velocity experiments described in the previous section were used to identify the parameters of the adopted friction model by deriving the static (both Coulomb and breakaway) and viscous friction variables of Eq. (4). An example of the resulting torque–velocity data recorded during one of the experiments for each of the tested prototypes is reported in Fig. 8. The mean and standard deviation values for the Coulomb, breakaway, and viscous friction factors of the C3D and CFB reducers are reported in Table 5. The best (i.e., the lower) values are marked in bold text.

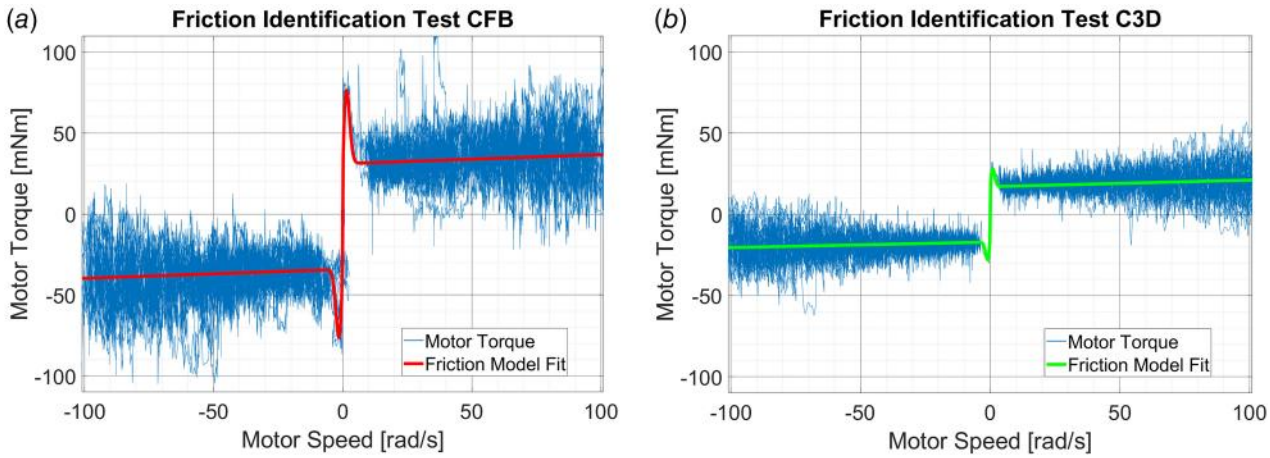

Fig. 8 Example of friction test results (motor torque over motor speed) for the CFB (*a*) and C3D (*b*) prototypes. The motor torque data are represented by the thin lines, while the fitted models are displayed in thicker lines for the CFB and C3D. The fitted Stribeck models portray distinctly the clear differences between the breakaway torques and the Coulomb static component.

Table 5 Results from the friction tests

ID	Breakaway friction (mN m)
CO30 [21]	$\mathbf{22.3 \pm 0.71}$
CFB	75.12 ± 0.61
C3D	27.59 ± 0.15
ID	**Coulomb friction (mN m)**
CO30 [21]	22.3 ± 0.71
CFB	31.55 ± 1.29
C3D	$\mathbf{16.39 \pm 0.72}$
ID	**Viscous factor (mN ms/rad)**
CO30 [21]	$0.91 \pm 0.11 \times 10^{-1}$
CFB	$0.59 \pm 0.11 \times 10^{-1}$
C3D	$\mathbf{0.37 \pm 0.08} \times 10^{-1}$

For the CO30 reducer from Ref. [21], the Coulomb static friction has been employed as a reference breakaway value.
Bold characters have been employed to highlight the best results.

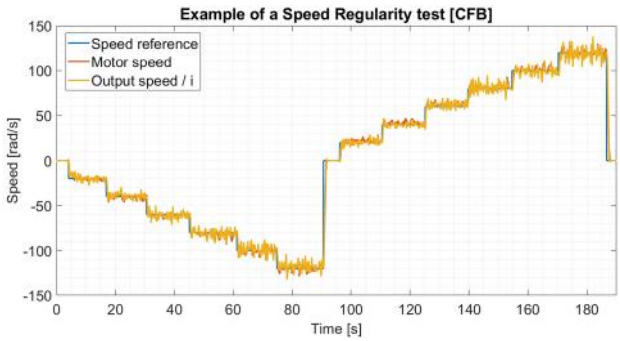

Fig. 9 Illustration of the results from a representative speed regularity experiment carried out on CFB. The reference input (the step fucntion) is a sequence of velocity steps ranging from 0 to 120 rad/s and then to −120 rad/s in steps of 20 rad/s. The additional traces correspond to the motor velocity and the reducer output velocity, the latter scaled by the transmission ratio *i* to allow direct visual comparison with the motor speed.

From these data, it is clear how the 3D-printed bearing structures embedded in the C3D reducer parts decisively improve both the static and viscous friction coefficients.

Furthermore, the results show how the fitted Stribeck friction for the C3D design displays better values than the ones reported for other state-of-the-art 3D-printed gearboxes [13,20,34] and transmission systems for lightweight assistive wearable exoskeletons, such as the one presented in Ref. [40], where the best reported values for static and viscous friction among the various mentioned works are, respectively, 11 mN m and 5 mN ms/rad.

3.5 Speed Regularity. Figure 9 shows an example of the data collected during a regularity test, with steps of 20 rad/s ranging from 0 to ±120 rad/s. The motor speed reference and the actual motor speed are plotted together with the reducer's output velocity rescaled by the reduction ratio i in order to better visualize the actual values on the same plot. For computing the regularity, the velocity transient phases from one step to another have been ignored, and only the regimen conditions have been employed. Table 6 presents the reducers' regularity values for the evaluated velocities. The best values for each velocity step are presented in bold characters.

The regularity data reported in Table 6 confirm that both the examined reducers exhibit consistently high performance across a wide range of motor speeds (20–120 rad/s), with total average regularity values (reported as R_{TOT}) above 96.7%. This indicates that all tested configurations—the reference CO30, CFB, and C3D—maintain stable output speed profiles, which is essential for reliable operation in wearable robotics. These regularity values approximately correspond to the best result from previous works [13,21], where other architectures displayed even significantly lower performance (regularities between 89.56% and 96.96%), confirming the high-quality results obtained by the tested prototypes and assessing the capability of the fully printed device to maintain valuable performances.

Notably, the best regularity values at each speed are highlighted in bold in the table, and the C3D reducer achieves the highest overall regularity ($R_{TOT} = 96.93\%$). Despite using fully 3D-printed sliding guides in place of conventional rolling bearings, the C3D maintains, and in some cases improves upon, the speed regularity compared to the other devices and the other gearboxes from Refs. [13,21]. This clearly demonstrates that the integration of 3D-printed compliant guiding structures does not degrade the system's kinematic consistency. The results validate the suitability of all the designs, and importantly, support the viability of low-cost, additively manufactured solutions like the C3D, which combine mechanical simplicity with competitive regularity performance.

3.6 Encumbrance, Weight, and Cost. Tables 7 and 8 reports the main dimensional and economic indicators of the three compound planetary reducers under comparison. The best values are marked in bold text. The different choice in the gear train tooth number has impacted favorably the weight, overall size, and cost. Thus, a definite improvement with respect to the prior design has been achieved. Moreover, while CO30 (1:30 reduction ratio) and the CFB prototype share a conventional architecture, where polymer gears are combined with standard steel rolling-element bearings, the fact that in the C3D prototype, the larger bearings are replaced with custom 3D-printed races and stainless-steel balls enables a predictable major decrease in size, mass, and cost. Specifically, the C3D external diameter and height are reduced by approximately 30% and 20% with respect to the reference design CO30, resulting in a total weight of 178 g, nearly half of the baseline 364 g and substantially lighter than the 261 g of the CFB. The adoption of the simplified 3D-printed bearing solution also yields a remarkable cost reduction, with the total expense dropping to less than 50€, compared to over 80€for the conventional baseline and about 70€for the CFB.

Concerning the axial expansion, the C3D prototype, despite displaying a definite improvement with respect to the previous CO30 and the CFB gearboxes, does not surpass the current state-of-the-art. This is a limitation due to the planetary compound architecture itself, since two planetary stages are disposed in series

Table 6 Regularity of the reducers at the investigated motor velocities

Motor speed (rad/s)	20	40	60	80	100	120	R_{TOT}
CO30 [21] regularity (%)	**97.86**	96.55	95.88	96.75	97.09	96.41	96.76
CFB regularity (%)	95.36	96.59	97.15	97.10	**97.24**	**97.08**	96.75
C3D regularity (%)	95.85	**97.07**	**97.26**	**97.31**	97.18	96.94	**96.93**

Table 7 Encumbrances of the presented reducers

ID	Diameter (mm)	Height (mm)
CO30 [21]	100	53.6
CFB	90	48.4
C3D	**70**	**43**

Table 8 Weight and cost of the presented reducers

ID	Weight (g)	Cost ()
CO30 [21]	364	83.17
CFB	261	70.23
C3D	**178**	**46.69**

axially. This constraint could be partially addressed by employing stronger printable materials, thus reducing the height of the planets and rings. Nevertheless, the C3D design displayed radial encumbrance, weight, and cost that outperform previous state-of-the-art 3D-printed reducers [13,20,21,27,30], despite most of them implementing lower reduction ratios (e.g., 11:1, 8:1). In these works, the best reported values for radial encumbrance, weight, and overall cost are, respectively, 78 mm, 184 g, and 51.34€. It should be noted that all these values, which are the lowest reported for a 3D-printed reducer in the literature, correspond to the CY80v1 from [21], a compact-cam cycloidal reducer. Additionally, C3D demonstrated strongly lower weights and radial encumbrances with respect to other gearboxes employed in hip assistive exoskeletons (such as the examples mentioned in Ref. [10], where, however, the authors do not report the actuators' prices). Additionally, according to the analysis performed in Ref. [41], where the authors review a wide variety of lower limb exoskeletons actuators analyzing the reducers' weights and reduction ratios, no reducers with a weight below 340 g have been reported in the literature. These considerations strongly enforce the future employment of the proposed gearboxes (especially C3D) in lightweight assistive wearable devices.

3.7 Conclusive Overview

3.7.1 Overall Performance Considerations. The presented comparative analysis highlights the advantages of the proposed reducer architectures with respect to existing 3D-printed and conventional designs. Both the CFB and C3D prototypes consistently demonstrated valuable improvements in key performance indicators, including gear play, backdrive torque, stiffness, friction, and overall compactness. In particular, the C3D design proved to be especially effective, achieving the lowest backdrive torque (0.42 ± 0.063 N m) and friction coefficients, while maintaining gear play values (0.195 ± 0.084 deg) comparable to the CFB prototype, despite the use of custom 3D-printed bearing structures.

Furthermore, the C3D reducer displayed clear advantages in weight (178 g), overall encumbrance, and cost (46.69€), outperforming both the prior baseline design and the CFB prototype. These aspects are particularly relevant for wearable assistive robotics, where compactness, backdriveability, low-friction, and low weight directly impact device ergonomics and user comfort. This confirms the suitability of the C3D architecture for transparent physical interaction.

Overall, the results validate the potential of compound planetary architectures with additively manufactured bearing elements as a promising direction for low-cost, lightweight, and high-performance actuators. The embedment of 3D-printed bearing systems in gearboxes not only decreases friction, encumbrance, mass, and cost—critical aspects in wearable robotics applications—but also enables a fully customized design while maintaining the same kinematic architecture.

3.7.2 Limitations. In this work, our goal was the evaluation of the effects of substituting classic metal-built bearings with customized polymeric races for steel rollers in 3D-printed gearboxes. Thus, the presented analysis focused on the key parameters that assess the value of a reduction gearbox, such as friction, backdriveability, regularity, and gear play. The next step, aiming for a complete validation of the employment of this structural solution in exoskeleton actuators, consists of carrying out a durability analysis of these 3D-printed bearings. Indeed, while in the literature various works focus on the life-cycle of printed gears [33,42–44] assessing their durability value, to the authors' knowledge, no previous examinations of 3D-printed bearings have been conducted. Considering the proven level of endurance of plastic gears, it is reasonable to think that the polymeric bearings could maintain sustained integrity, given the difference in solicitation with respect to the teeth of the gearing components. However, a systematic analysis must be conducted to definitely prove these considerations. Therefore, given the definitely beneficial effect that 3D-printed polymeric races have demonstrated on the reducer's performance, it will be fundamental to carry out an extensive experimental evaluation of the printed races' resistivity.

4 Conclusions and Future Works

In this work, we presented the design, prototyping, and evaluation of two open-source 3D-printed compound planetary reducers conceived for lightweight and cost-effective wearable robots. The first implementation (CFB) followed a conventional configuration with standard steel bearings, while the second (C3D) introduced a novel solution based on an integrated custom 3D-printed bearing guides. This design choice led to a substantial reduction in friction, backdriveability, weight, and manufacturing cost compared to state-of-the-art 3D-printed and metal-built reducers designed for robotics and assistive exoskeletons applications, while maintaining valuable levels of stiffness and speed regularity. The comparative experimental assessment highlighted how the introduction of printed bearing systems offers a promising alternative for lightweight and cost-effective actuation in assistive exoskeletons.

Future work will focus on several directions. First, a more comprehensive analysis of long-term reliability and wear will be carried out to definitely validate the applicability of the proposed reducers in actual exoskeletons. Then, a systematic exploration of different printable materials will be undertaken to optimize both gears and bearing components, to enhance durability and compactness. Moreover, the application of the 3D-printed bearings paradigm to other transmission architectures, such as cycloidal reducers, will be considered to reach even lower weights and encumbrances. Finally, future efforts will focus on integrating the proposed reducers into a wearable assistive exoskeleton, in order to experimentally validate their effectiveness in real-world human–robot interaction scenarios.

Funding Data

- The purchase of the materials used in this work and part of the personnel costs were supported by the BRIEF "Biorobotics Research and Innovation Engineering Facilities" project (project identification code IR0000036) funded under the National Recovery and Resilience Plan (NRRP) and Mission 4 Component 2 Investment 3.1 of the Italian Ministry of University and Research funded by the European Union—NextGenerationEU. Part of the activities and of the personnel of this work were supported by the Department of Excellence

in Robotics and AI, funded by the Ministry of Research and University (DM 230/2022).

Conflict of Interest

There are no conflicts of interest.

Data Availability Statement

The datasets generated and supporting the findings of this article are obtainable from the corresponding author upon reasonable request.

References

[1] Proietti, T., Ambrosini, E., Pedrocchi, A., and Micera, S., 2022, "Wearable Robotics for Impaired Upper-Limb Assistance and Rehabilitation: State of the Art and Future Perspectives," IEEE Access, **10**, pp. 106117–106134.

[2] Karthik, V., Das, S., Nayak, S., and Pandey, A., 2025, "Lower Limb Exoskeletons, Application-Centric Classifications: A Review," J. Field Rob., **42**(6), pp. 2397–2411.

[3] Zhu, L., Cui, C., Zhang, D., Tan, J., and Xu, C., 2024, "Modeling and Control of Cable-Driven Exoskeleton for Arm Rehabilitation," ASME J. Mech. Rob., **17**(6), p. 061010.

[4] Laschowski, B., and McPhee, J., 2023, "Energy-Efficient Actuator Design Principles for Robotic Leg Prostheses and Exoskeletons: A Review of Series Elasticity And Backdrivability," ASME J. Comput. Nonlinear Dyn., **18**(6), p. 060801.

[5] Hunt, J., and Lee, H., 2018, "A New Parallel Actuated Architecture for Exoskeleton Applications Involving Multiple Degree-of-Freedom Biological Joints," ASME J. Mech. Rob., **10**(5), p. 051017.

[6] Bezzini, R., Avizzano, C. A., Porcini, F., and Filippeschi, A., 2024, "Transparency Evaluation for the Kinematic Design of the Harnesses Through Human-Exoskeleton Interaction Modeling," IEEE/RSJ International Conference on Intelligent Robots and Systems (IROS), Abu Dhabi, UAE, Oct. 14–18, pp. 9335–9341.

[7] Qian, Y., Han, S., Wang, Y., Yu, H., and Fu, C., 2022, "Toward Improving Actuation Transparency and Safety of a Hip Exoskeleton With a Novel Nonlinear Series Elastic Actuator," IEEE/ASME Trans. Mechatron., **28**(1), pp. 417–428.

[8] Calanca, A., Toxiri, S., Costanzi, D., Sartori, E., Vicario, R., Poliero, T., Di Natali, C., Caldwell, D. G., Fiorini, P., and Ortiz, J., 2020, "Actuation Selection for Assistive Exoskeletons: Matching Capabilities to Task Requirements," IEEE Trans. Neural Syst. Rehabil. Eng., **28**(9), pp. 2053–2062.

[9] Huang, T.-H., Zhang, S., Yu, S., MacLean, M. K., Zhu, J., Di Lallo, A., Jiao, C., Bulea, T. C., Zheng, M., and Su, H., 2022, "Modeling and Stiffness-Based Continuous Torque Control of Lightweight Quasi-direct-drive Knee Exoskeletons for Versatile Walking Assistance," IEEE Trans. Rob., **38**(3), pp. 1442–1459.

[10] Yu, S., Huang, T.-H., Yang, X., Jiao, C., Yang, J., Chen, Y., Yi, J., and Su, H., 2020, "Quasi-direct Drive Actuation for a Lightweight Hip Exoskeleton With High Backdrivability and High BandWidth," IEEE/ASME Trans. Mechatron., **25**(4), pp. 1794–1802.

[11] Barsomian, C., Eswaran, N., Pesenti, M., Gandolla, M., Braghin, F., Carpanzano, E., and Roveda, L., 2024, "Dynamic Characterization and Control of a Back-Support Exoskeleton 3D-Printed Cycloidal Actuator," CIRP Ann., **73**(1), pp. 29–32.

[12] Jenks, B., Levan, H., and Stefanovic, F., 2025, "OpenSEA: A 3D Printed Planetary Gear Series Elastic Actuator for a Compliant Elbow Joint Exoskeleton," Front. Rob. AI, **12**, p. 1528266.

[13] Bezzini, R., Bassani, G., Alberto Avizzano, C., and Filippeschi, A., 2025, "Design of a Novel Flat Cycloidal-Planetary Series Reducer and Experimental Assessment for Assistive Exoskeletons Actuation-CYPLO," IEEE Access, **13**, pp. 202619–202631.

[14] Zhang, Y., Bressel, M., De Groof, S., Dominé, F., Labey, L., and Peyrodie, L., 2023, "Design and Control of a Size-Adjustable Pediatric Lower-Limb Exoskeleton Based on Weight Shift," IEEE Access, **11**, pp. 6372–6384.

[15] Guida, R., Bertolino, A. C., De Martin, A., and Sorli, M., 2025, "A New Computationally Efficient Model of the Non-Linear Dynamics in Harmonic Drive Reducers," Mech. Mach. Theory, **209**, p. 105992.

[16] Fujiwara, T., Nagano, K., and Wada, M., 2024, "Torque-Sensorless Impedance Control for an Actuator With Compound Planetary Gearbox for Reducing External Contact Force," 2024 IEEE/ASME International Conference on Advanced Intelligent Mechatronics (AIM), Boston, MA, July 15–19, IEEE, pp. 741–746..

[17] Matsuki, H., Nagano, K., and Fujimoto, Y., 2019, "Bilateral Drive Gear—A Highly Backdrivable Reduction Gearbox for Robotic Actuators," IEEE/ASME Trans. Mechatron., **24**(6), pp. 2661–2673.

[18] Hur, S., Kim, D., Lee, C., and Choi, D., 2023, "Optimal Design of a Compound Planetary Reducer Using a Nonlinear Optimization Method," IEEE Access, **11**, pp. 7822–7828.

[19] Roozing, W., and Volbeda, J., 2025, "Anti-Backlash Mechanisms for Cycloidal Drive Robotic Actuators: Design and Evaluation," IEEE Rob. Autom. Lett., **10**(11), pp. 12221–12228.

[20] Satake, H., and Takesue, N., 2024, "Comparison of Characteristics of Cycloidal Gear Reducer Using Metal, Plastic and 3D Printed Parts," 2024 IEEE/SICE International Symposium on System Integration (SII), Ha Long, Vietnam, Jan. 8–11, IEEE, pp. 1531–1536.

[21] Bezzini, R., Bassani, G., Avizzano, C. A., and Filippeschi, A., 2024, "Design and Experimental Evaluation of Multiple 3D-Printed Reduction Gearboxes for Wearable Exoskeletons," Robotics, **13**(11), p. 168.

[22] Mourya, V., Bhore, S. P., and Wandale, P. G., 2023, "Comparative Investigation on Wear Properties of 3D-Printed Textured Journal Bearings," J. Manuf. Process., **103**, pp. 337–353.

[23] Lee, Y.-J., Lee, K.-H., and Lee, C.-H., 2018, "Friction Performance of 3D Printed Ball Bearing: Feasibility Study," Results Phys., **10**, pp. 721–726.

[24] Moldovan, C., and Sticlaru, C., 2023, "Performance Analysis of Polymer Additive Manufactured Gear Bearings," Appl. Sci., **13**(22), p. 12383.

[25] Kam, M., Saruhan, H., and İpekçi, A., 2023, "Experimental Investigation of Vibration Damping Capabilities of 3D Printed Metal/Polymer Composite Sleeve Bearings," J. Thermopl. Compos. Mater., **36**(6), pp. 2505–2522.

[26] Doğan, B. K., Dal, A., Ağören, G., and Karaçay, T., 2024, "Vibration Behavior of a 3D-Printed Hybrid Polymer Bearing With Outer Race Defect," Ind. Lubr. Tribol., **76**(2), pp. 299–306.

[27] Roozing, W., and Roozing, G., 2024, "Experimental Comparison of Pinwheel and Non-Pinwheel Designs of 3D-Printed Cycloidal Gearing for Robotics," 2024 IEEE International Conference on Robotics and Automation (ICRA), Yokohama, Japan, May 13–17, IEEE, pp. 7091–7098.

[28] Xu, S., Tang, K., Xu, L., and Ding, Y., 2024, "Design, Analysis, and Validation of a Passive Parallel Continuum Ankle Exoskeleton for Support and Walking Assistance," J. Mech. Rob., **17**(3), p. 031003.

[29] Bezzini, R., 2025, "Fully 3D-Printed Compound Planetary 30:1 Gearbox," https://github.com/RicBez/3D-printed-bearings-30-1-compound-reducers.git, GitHub repository [Online, Available].

[30] Yoshida, T., Endo, G., Okubo, A., and Nabae, H., 2023, "Experimental Evaluation of a Quasi-Direct-Drive Actuator With a 3D-Printed Planetary Gear Reducer," 2023 IEEE/SICE International Symposium on System Integration (SII), Atlanta, GA, Jan. 17–20, IEEE, pp. 1–6.

[31] Kapelevich, A., and AKGears, L., 2013, "High Gear Ratio Epicyclic Drives Analysis," Ratio, **3**(10), pp. 1–12.

[32] Buj-Corral, I., and Zayas-Figueras, E. E., 2023, "Comparative Study About Dimensional Accuracy and Form Errors of FFF Printed Spur Gears Using PLA and Nylon," Polym. Test., **117**, p. 107862.

[33] Ciobanu, R., Arhip, G., Donţu, O., Rizescu, C. I., and Grămescu, B., 2025, "Additive Manufacturing Meets Gear Mechanics: Understanding Abrasive Wear Evolution in FDM-Printed Gears," Polymers, **17**(13), p. 1810.

[34] Roozing, W., and Roozing, G., 2022, "3D-Printable Low-Reduction Cycloidal Gearing for Robotics," 2022 IEEE/RSJ International Conference on Intelligent Robots and Systems (IROS), Kyoto, Japan, Oct. 23–27, IEEE, pp. 1929–1935.

[35] Zhang, Q., Nalam, V., Tu, X., Li, M., Si, J., Lewek, M. D., and Huang, H. H., 2022, "Imposing Healthy Hip Motion Pattern and Range by Exoskeleton Control for Individualized Assistance," IEEE Rob. Autom. Lett., **7**(4), pp. 11126–11133.

[36] Kang, I., Hsu, H., and Young, A., 2019, "The Effect of Hip Assistance Levels on Human Energetic Cost Using Robotic Hip Exoskeletons," IEEE Rob. Autom. Lett., **4**(2), pp. 430–437.

[37] Satheeshbabu, S., Puduchatiram Raman, E., Krishnan, G., and Patiballa, S. K., 2025, "Design of Compliant Systems With Embedded Actuation (CoSEA)," ASME J. Mech. Rob., **17**(12), p. 121003.

[38] Sandeep Reddy, M., Rakshit, S., and Sujatha, S., 2025, "A New Adjustable Stiffness Rotary Series Elastic Actuator Based on Lockable Spring Elements," ASME J. Mech. Rob., **17**(12), p. 121005.

[39] Hussain, I., Turki Almansoori, M., Tamaizi, K., Albalasie, A., Niu, Z., and Gan, D., 2026, "Design, Modeling, Evaluation, and Control of a Compact Discrete Variable Stiffness Actuator," ASME J. Mech. Rob., **18**(2), p. 020903.

[40] Seiler, J., Schêfer, N., Zhao, G., Latsch, B., Grimmer, M., Beckerle, P., and Kupnik, M., 2024, "Human-Exoskeleton Interaction Force Estimation Based on Quasi-direct Drive Actuators," 2024 10th IEEE RAS/EMBS International Conference for Biomedical Robotics and Biomechatronics (BioRob) , Heidelberg, Germany, Sept. 1–4, IEEE, pp. 1132–1139.

[41] Bettella, F., Tortora, S., Menegatti, E., Petrone, N., and Del Felice, A., 2025, "A Scoping Review on Lower Limb Exoskeleton Actuation'S Description and Characteristics," Robotica, **43**(4), pp. 1–18.

[42] Tunalioglu, M. S., and Agca, B. V., 2022, "Wear and Service Life of 3-D Printed Polymeric Gears," Polymers, **14**(10), p. 2064.

[43] Ciobanu, R., Rizescu, C. I., Rizescu, D., and Gramescu, B., 2024, "Surface Durability of 3D-Printed Polymer Gears," Appl. Sci., **14**(6), p. 2531.

[44] Doğan, O., and Kamer, M. S., 2025, "Wear Characteristics of 3D-Printed Spur Gears: Material Type and Design Parameters Effects," Iranian Polym. J., **34**(9), pp. 1399–1413.